Supplementary material

Lattice sites of implanted Na in GaN and AlN and comparison to other light alkalis and alkaline earths

U. Wahl, E. David-Bosne, L. M. Amorim, A. C. Costa, B. De Vries, J. G. Correia, M. R. da Silva, L. M. C. Pereira , and A. Vantomme

Note: references are with respect to those in the original article

1. Additional information on sample characteristics

Table SI mentions additional details from sample characterization using Rutherford Backscattering Spectrometry/Channeling (RBS/C) and X-Ray Diffraction (XRD). In case of AlN, the RBS/C (Fig. S1) and XRD (Fig. S2) characterization was performed on a sample cut from the same wafer as the one used in the emission channeling experiment, while for GaN #1 and GaN #2 typical values for batches of samples from the same grower/supplier are mentioned.

TABLE SI. Additional information on structural characterization of the samples and type of detector used for emission channeling measurements.

Sample	GaN #1	GaN #2	AlN
Internal number	#472	#199	#193/201
Year of growth/purchase	2014	1998	2002
Growth method	MOVPE (U Cambridge)	MOVPE (Cree Inc.)	MOVPE (U Montpellier)
Film thickness (μm)	4.8	1.5	0.28
Buffer layer / substrate	sapphire	sapphire	0.55 μm $Al_{0.2}Ga_{0.8}N$ / sapphire
RBS/C χ_{min} [0001]		2%	21% [a]
W_{tilt}	0.07° [b]	0.1°	0.20° [a]
W_{twist}	0.08° [b]	0.2°	0.56° [a]
Detector	pad #6 + Timepix	pad #4	pad #2

[a] From [33]
[b] M. Kappers, private communication

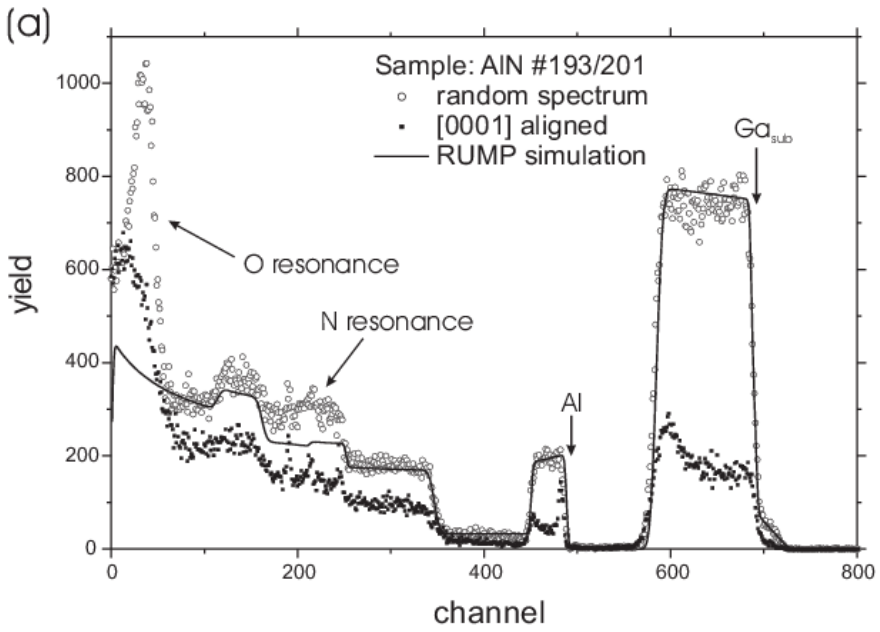

FIG S1. Random and aligned RBS spectra for a virgin AlN sample taken from wafer #193/201. The spectra were acquired using 3.5 MeV $^4He^{2+}$ ions. At this energy, the Al signal (channels 450-500) and the Ga signal from the buffer layer (channels 580-700) are clearly resolved. The analysis shows that the buffer layer between the AlN and the sapphire is not pure GaN, but $Al_{0.2}Ga_{0.8}N$, which has a thickness of around 5500 Å. The AlN layer itself has a thickness of 2800 Å and shows a contamination with about 4% of Ga near the interface with the buffer layer. This gallium content is probably due to residual Ga-containing gases still present in the growth chamber during the growth of the AlN layer. However, up to a depth of several hundreds of Å from the surface, which corresponds to the ion implanted region in emission channeling experiments, the layer consists of pure AlN. From [33].

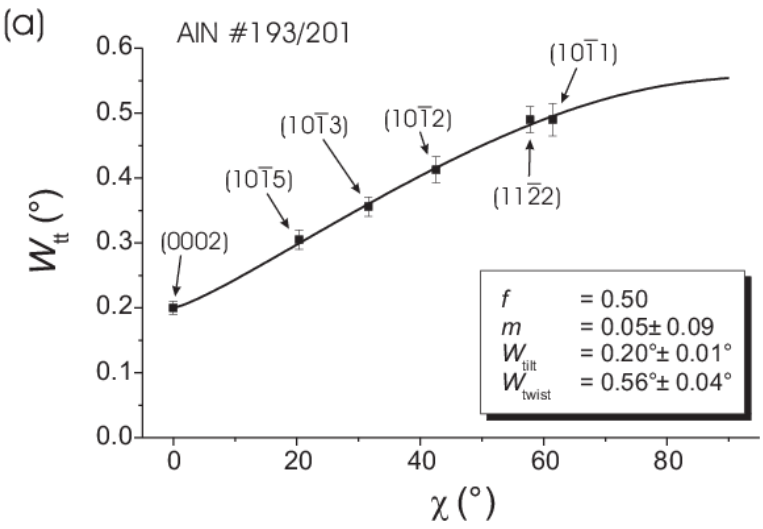

FIG S2. FWHM W_{tt} of the XRD skew-symmetric rocking curves as a function of inclination angle χ for AlN wafer #193/201, as determined from fitting XRD lines with pseudo-Voigt functions. The full line is a fit of the experimental data using the model of Srikant et al., i.e. equation (3) of Ref. [31]. While the tilt component W_{tilt} of the mosaic spread is directly obtained from the FWHM of the (0002) reflection, the twist value W_{tilt} is the one extrapolated for χ=90°. From [33].

2. Background correction

Electron emission channeling experiments are generally subject to two sources of background which add approximately flat contributions to the measured patterns and need to be corrected during the analysis: a) backscattering of electrons towards the detector from inside the sample, the sample holder, and the walls of the vacuum chamber, b) detection of gamma particles. The background from backscattered electrons can be estimated theoretically with the help of GEANT4 Monte Carlo simulations taking into account the ^{24}Na β energy distribution (Fig. S3) and the geometry and materials of the sample and setup. On the other hand, the background from γ radiation can be estimated experimentally from the residual count rate after closing a shutter in front of the detector. The effects of backscattered electrons and gamma background were thus taken into account by multiplying all derived site fractions with correction factors that are specific for each experiment and detector used, with values ranging from 1.74-3.15 for backscattered electrons, and 1.17 for gamma background. Note that, while the substitutional and interstitial fractions of ^{24}Na can be determined relatively to each other with very good precision, due to the approximate nature of the background correction procedure the absolute accuracy of fractions is less, with absolute errors in the sum of both fractions estimated at ~10%.

3. Many-beam simulations

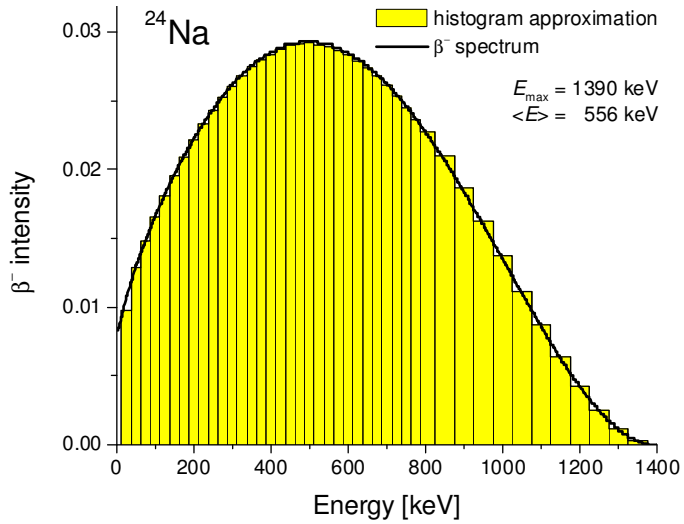

FIG S3. Histogram of the energy values used to approximate the β^- spectrum of ^{24}Na in the "many-beam" calculations.

In order to quantitatively analyze the experimental electron emission distributions, they were fitted by linear combinations of theoretical emission patterns for various lattice sites, which were calculated using the "many-beam" formalism for electron channeling [17, 18]. ^{24}Na decays by the emission of β^- particles with an endpoint energy of 1.39 MeV (average β^- energy 556 keV). To account for the continuous β^- spectrum, "many-beam" simulations were performed for a number of discrete electron energies (step widths of 25 keV in the energy range 25-800 keV, 50 keV in the range 800-1400 keV) and weighted according to the β^- spectrum of ^{24}Na (Fig. S3). The number of "beams" used in the simulations was 16 in the energy range 25-725 keV, 20 for 750-950 keV, and 24 for 1000-1400 keV. Angular patterns were calculated in *x*- and *y*-direction from −3° to +3° in steps of 0.025° for GaN, 0.050° for AlN and for 200-250 different lattice sites in the wurtzite structure. The designations and positions of the major sites of highest symmetry are shown in Fig. S4. The SA, SB, T, ABA(c), O, HA, HB, and HAB site patterns are shown on the following pages in Figs S5-S6 for GaN and Figs S7-S8 for AlN.

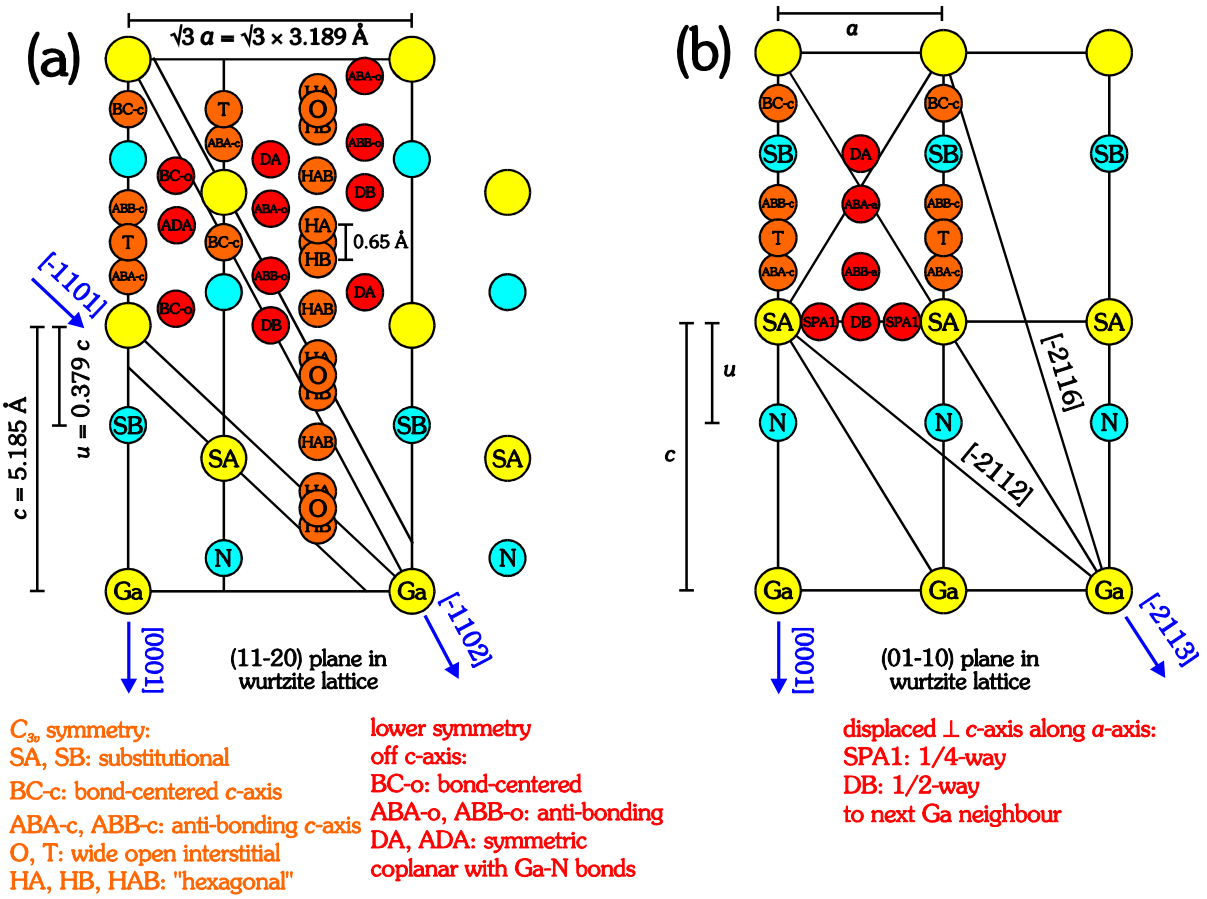

FIG. S4. The (11–20) (a) and (01–10) (b) planes of the GaN wurtzite lattice, showing the substitutional cation SA (Ga or Al) and anion SB (N) sites, as well as the following interstitial sites: bond center BC, anti-bonding AB, tetrahedral T, hexagonal H and octahedral O. The addition of "A" or "B" to the site name indicates non-equivalent sites closer to the cation A or the anion B, respectively, e.g. the hexagonal sites HA and HB. On the other hand, the interstitial T, O and HAB sites are defined as having the same distance from A and B sites (i.e. located exactly at the center in between planes of A and B atoms). "-c" indicates BC or AB sites located within the atomic rows along the *c*-axis, while those indicated with "-o" are basal to it. Note that O, HA, HB , and HAB sites are outside the (01–10) atomic planes and hence not visible in panel (b). The directions around which the β^- angular emission yield from ^{24}Na was measured are represented by the vectors shown in blue. The values indicated for the lattice constants *a* and *c* as well as for the bond length parameter *u* are those of GaN.

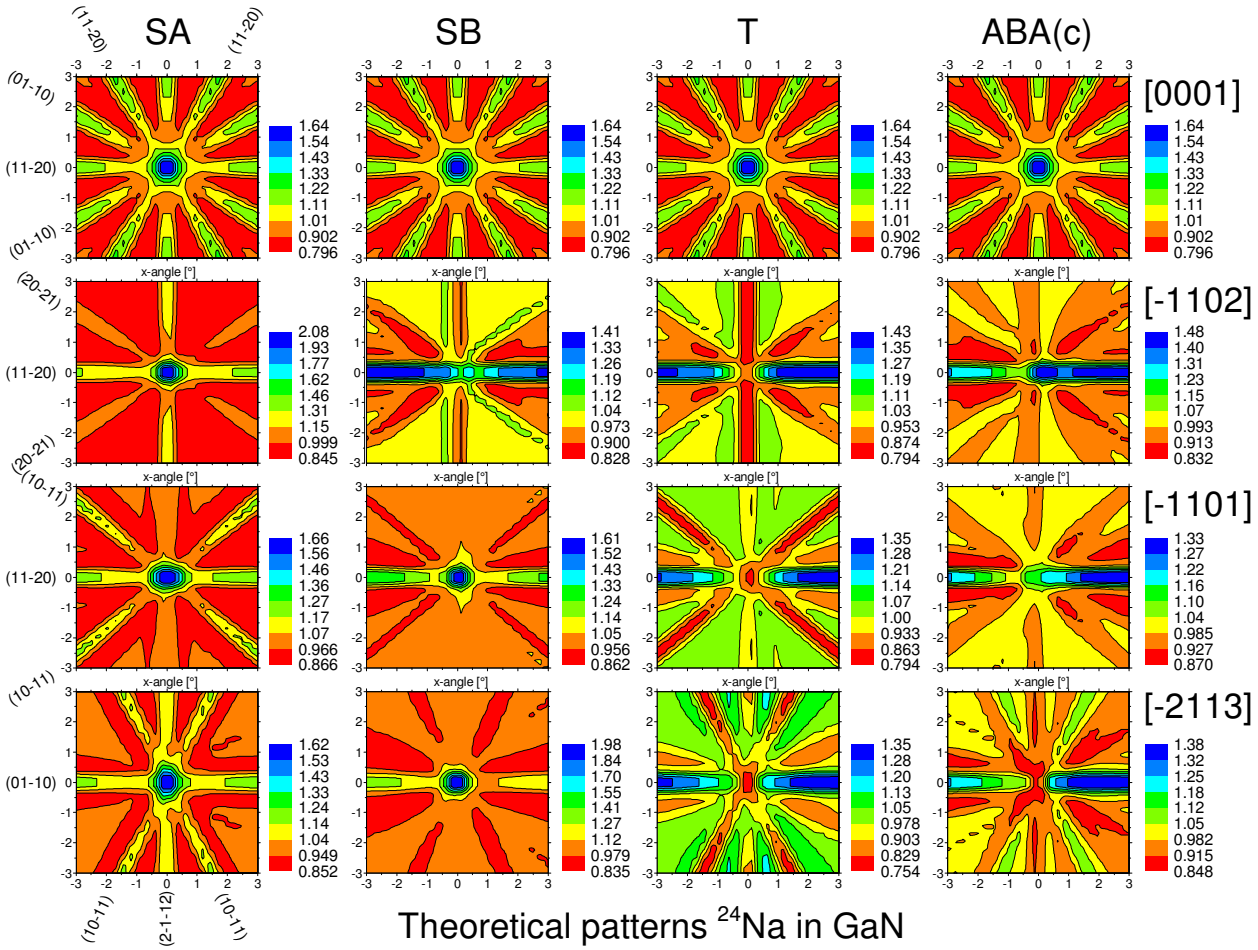

FIG S5. Theoretical β^- emission patterns from ^{24}Na on substitutional Ga (SA), substitutional N (SB), tetrahedral interstitial T and ABA(c) sites around the [0001], [–1102], [–1101], and [–2113] axes of GaN. Note that all of these sites are aligned with the *c*-axis atomic rows, so their [0001] patterns are all identical. The patterns were calculated assuming a ^{24}Na implantation profile of 422(209) Å and are shown with the angular resolution of 0.10° (standard deviation) and the azimuthal orientation of the pad detector measurements of GaN sample #1 (ϕ_0=180°).

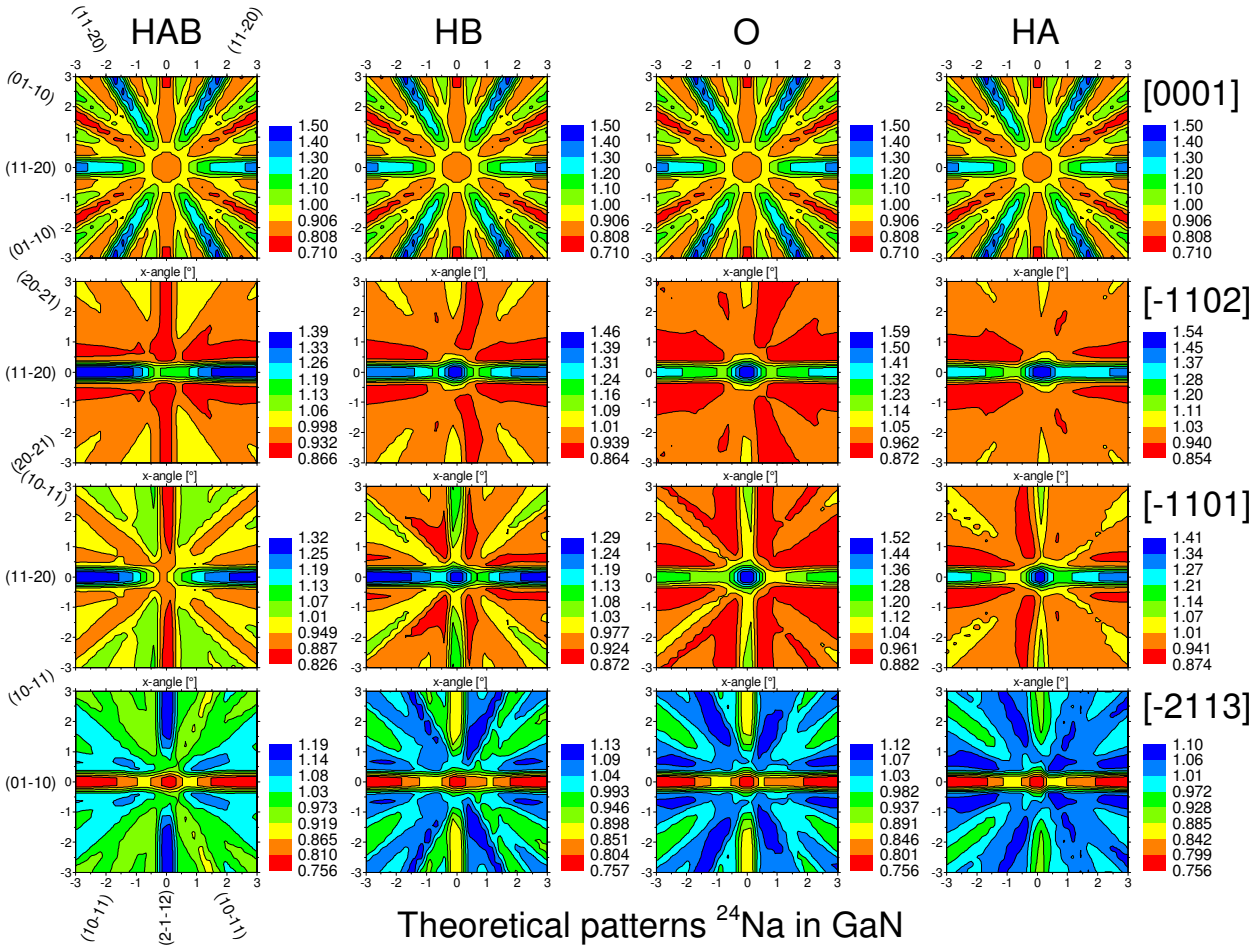

FIG S6. Theoretical β^- emission patterns from ^{24}Na on interstitial HAB, HB, O and HA sites around the [0001], [–1102], [–1101], and [–2113] axes of GaN. Note that with respect to the *c*-axis, all of these sites are located in the wide open interstitial region, so their [0001] patterns are all identical. The patterns were calculated assuming a ^{24}Na implantation profile of 422(209) Å and are shown with the angular resolution of 0.1° (standard deviation) and the azimuthal orientation of the pad detector measurements of GaN sample #1 (ϕ_0=180°).

Note that the [0001] and [–2113] axes are the two directions that best allow identifying the occupation of interstitial O sites also by visual inspection. This is due to the fact that along both of these directions O sites are not aligned with the atomic rows (cf. Fig. S4), thus causing axial "blocking" dips rather than channeling maxima. Both directions also intersect with (01–10) planes, which also show blocking effects. In contrast, interstitial O sites are approximately aligned with the [–1102] and [–1101] axes, as is visible from Fig. S4 or from Fig. 1 of the main paper. Hence, the occupation of O sites will produce channeling effects along [–1102] and [–1101], which are similar to (but not the same) as those resulting from substitutional Ga sites , thus making distinction of S and O sites not obvious "to the naked eye".

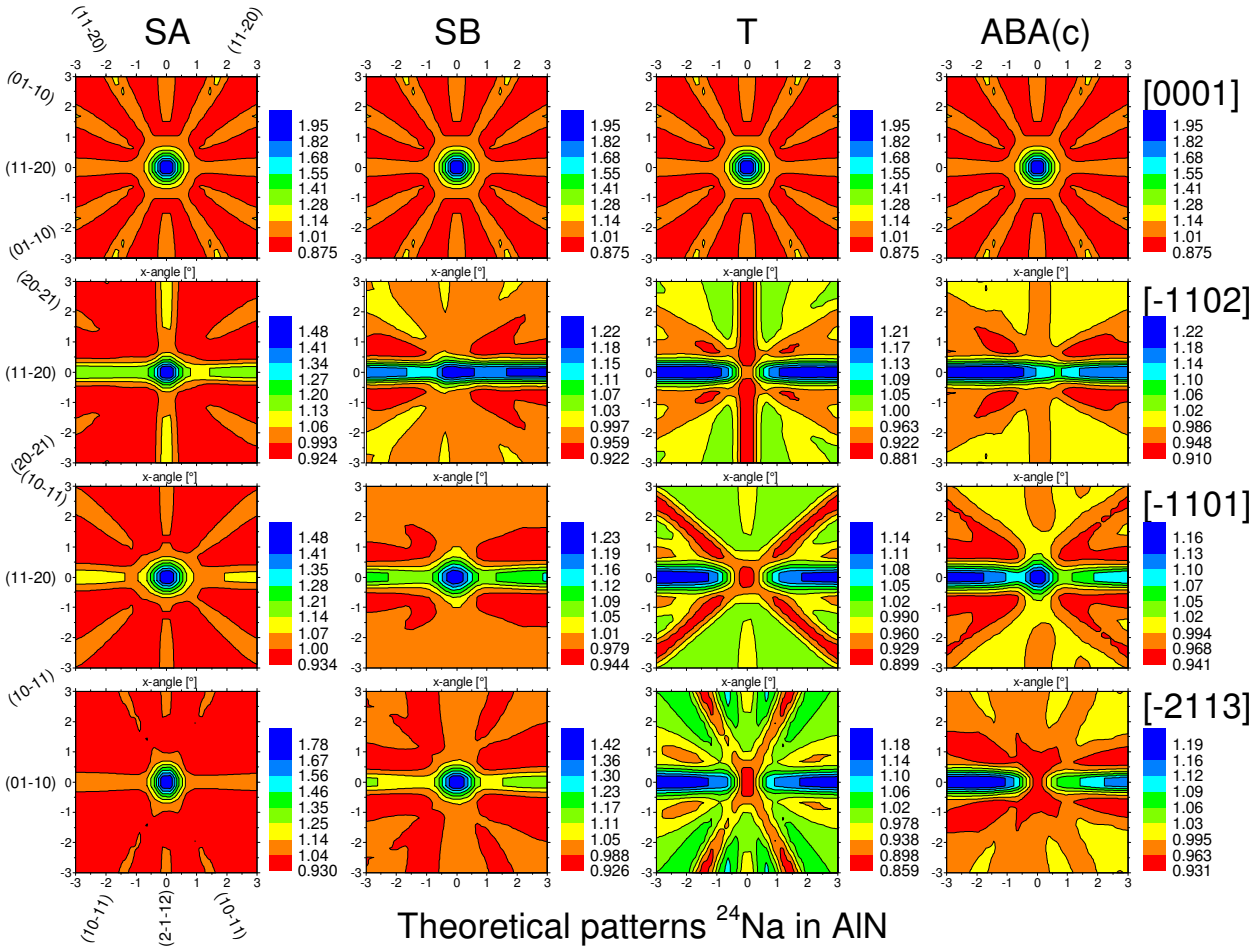

FIG S7. Theoretical β^- emission patterns from ^{24}Na on substitutional Al (SA), substitutional N (SB), tetrahedral interstitial T and ABA(c) sites around the [0001], [–1102], [–1101], and [–2113] axes of AlN. Note that all of these sites are aligned with the *c*-axis atomic rows, so their [0001] patterns are all identical. The patterns were calculated assuming a ^{24}Na implantation profile of 825(300) Å. They are shown with angular resolutions (standard deviations) that, in addition to the diameter of the beam spot and the detector position resolution, also take into account the mosaic spread of the AlN sample, i.e. with 0.15° for [0001], 0.20° for [–1102], 0.25° for [–1101], and 0.20° for [–2113]. The azimuthal orientations correspond to the measurements of the AlN sample (ϕ_0=0°).

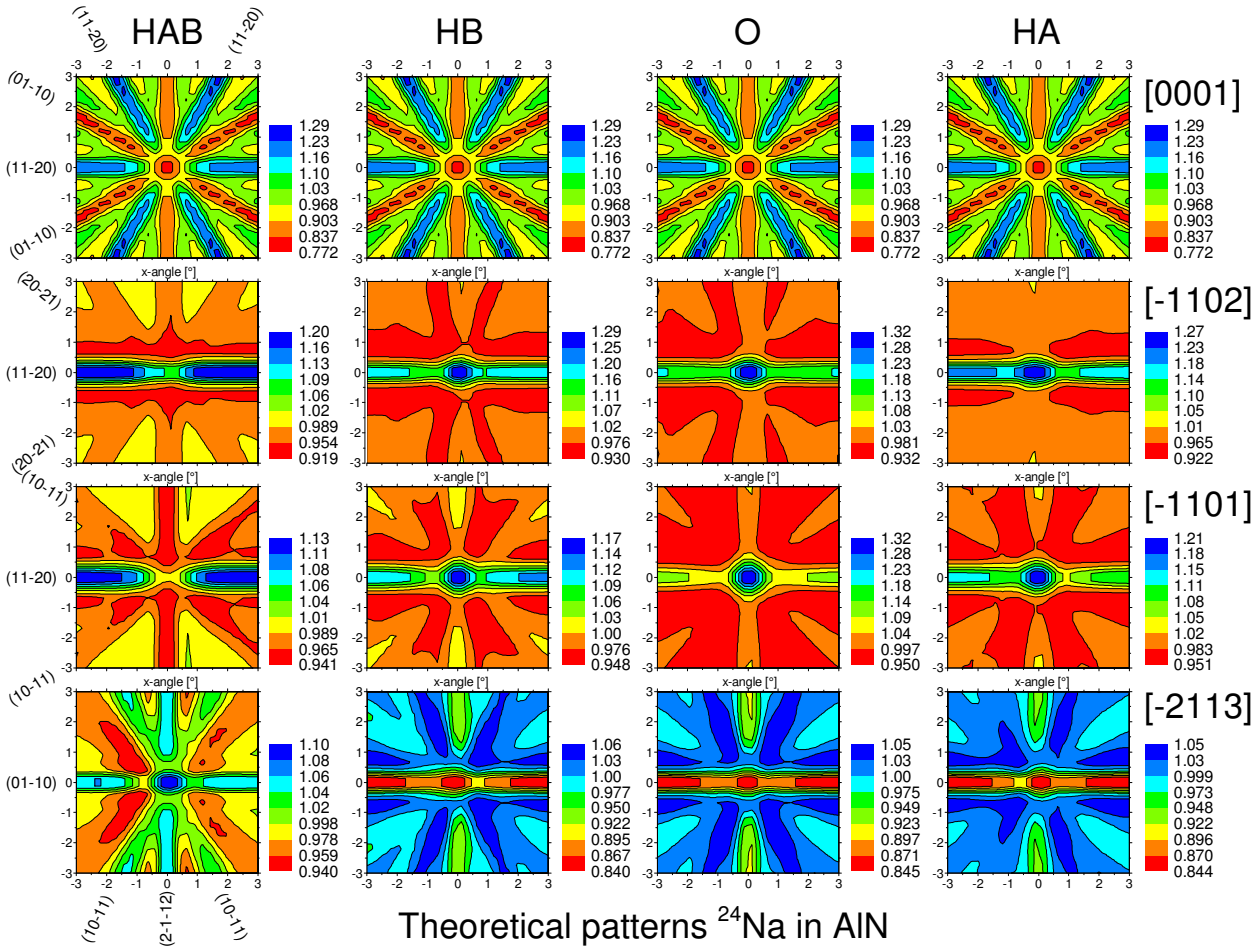

FIG S8. Theoretical β^- emission patterns from ^{24}Na on interstitial HAB, HB, O and HA sites around the [0001], [–1102], [–1101], and [–2113] axes of AlN. Note that with respect to the *c*-axis, all of these sites are located in the wide open interstitial region, so their [0001] patterns are all identical. The patterns were calculated assuming a ^{24}Na implantation profile of 825(300) Å. They are shown with angular resolutions (standard deviations) that, in addition to the diameter of the beam spot and the detector position resolution, also take into account the mosaic spread of the AlN sample, i.e. with 0.15° for [0001], 0.20° for [–1102], 0.25° for [–1101], and 0.20° for [–2113]. The azimuthal orientations correspond to the measurements of the AlN sample (ϕ_0=0°).

4. Additional comments on experimental patterns from GaN sample #1 in Figs 2 and 3 of main paper

The background of gamma particles that this pad detector #6 measures is not completely flat but varies by ~15%, due to an inhomogeneous detector response to gamma particles. This is mostly due to the fact that the detector is not run fully depleted, so that its depletion thickness (and hence detection efficiency for gamma particles) varies, probably according to slight variations of the Si substrate doping level. Running the detector not fully depleted greatly helps in reducing the gamma background from ^{24}Na, which only amounts to ~14% of the whole count rate under these conditions while for a fully depleted detector it could be as high as 40% [21]. However, in this case lowering the background comes at the cost of making it somewhat inhomogeneous. Overall, the anisotropy of the measured patterns is only affected at the ~2% level.

These variations are present in all patterns for GaN sample #2 that were measured with this detector. In Figs 2(b)-(d) and Figs 3 (a)-(d) of the main paper, they occur in between left (higher gamma count rate) and right (lower gamma count rate). The [0001] pattern shown in Fig. 2(a) of the main paper was the first measurement of the sample when the (11–20) plane was not yet oriented horizontally, hence for easier comparison with the other patterns, we have rotated it by 90 deg counter-clockwise. This means the gamma background is lower in the upper part and higher in the lower part.

The inhomogeneous background cannot be taken into account in the fitting procedure and thus decreases the best match that can be reached between experimental data and the fit. However, this does not affect the identification of the most probable lattice site. This can be seen from the fact that the measurements of the same sample with the Timepix detector, which does not suffer from this effect, yield very similar results, cf. Fig. 6 of the main paper.

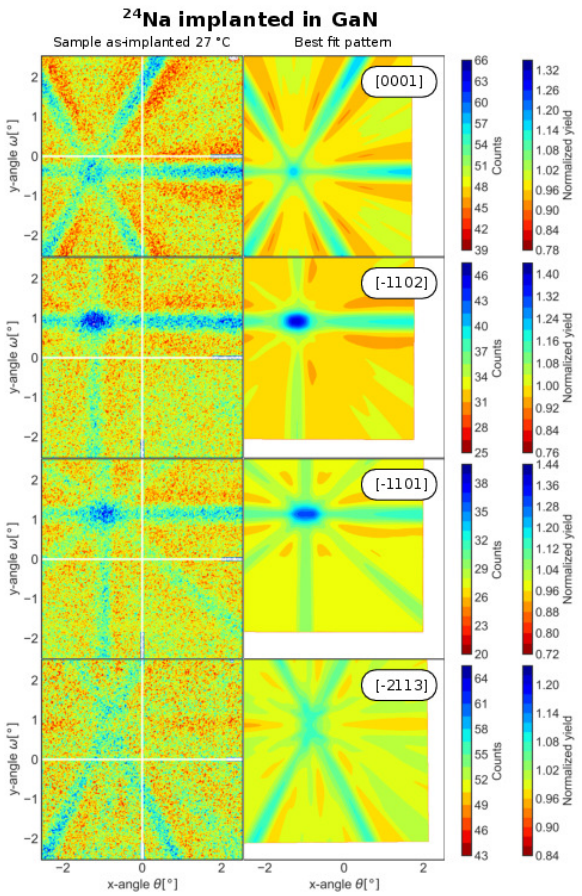

FIG. S9. Left column: angular distribution of β^- emission yields from ^{24}Na in GaN sample #1, measured at RT as-implanted with the Timepix detector. Patterns are shown as matrix plots around the [0001], [–1101], [–1102] and [–2113] axes. The cross shown in white and centered in the patterns corresponds to regions where the four readout chips of the detector join and where therefore are no useful pixels. The approximate numbers of events measured were 9.0×10^6 (a), 4.7×10^6 (b), 5.8×10^6 (c), and 9.6×10^6 (d). The color bars indicate the number of counts per bin of 2×2 pixels and the corresponding normalized yield. Right column: the best fit of simulated patterns, corresponding to 38% on Na_i interstitial and 32% on S_{Ga} sites. 32% -0.24 8.2

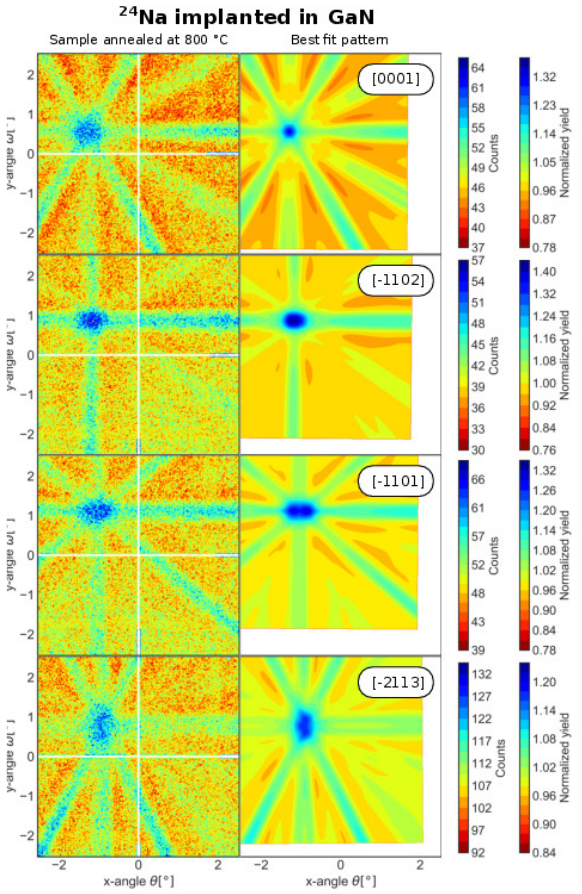

FIG. S10. (a)-(d): Same as Fig. 4 but measured following annealing at T_A=800°C. The approximate numbers of events measured were 8.4×10^6 (a), 8.3×10^6 (b), 6.8×10^6 (c) and 1.9×10^7 (d). The left column are experimental patterns while the right column shows the best fit of simulated patterns, corresponding to 15% on Na_i interstitial and 49% on S_{Ga} sites.

5. Measurement results of GaN sample #1 with the highly pixelated Timepix detector

Highly pixelated Timepix detectors [24-25] are intended as replacements for the pad detectors [23], which are now in service for about 20 years and no longer in production. While Timepix detectors, due to their large number of pixels (512×512 pixels of 55 µm size), provide significantly better position resolution than pad detectors (22×22 pixels of 1.3 mm size), the smaller pixel size does not translate into an equivalent improvement in angular resolution, since the latter is still limited by the 1 mm diameter of the radioactive beam spot on the sample. With both detectors mounted at a distance of 30 cm from the sample, the angular resolutions are 0.081° (standard deviation) for the pad geometry and 0.050° for the Timepix [26]. Due to the better angular resolution, more details of the patterns are resolved by the Timepix, however, with much lower number of counts/pixel.

In order to compare the performance of the two detector types and the outcome of the respective analysis procedures, besides using a pad detector, GaN sample #1 was also measured with the Timepix (Fig. S9 above, as-implanted, Fig. S10, above, following annealing). Since the characteristics of the measured patterns regarding number of pixels, events/pixel, angular resolution, response to background, etc. of the two detectors are rather different, the added value brought by performing both types of measurements is showing that the identification of most probable Na lattice sites and the spread in the most probable positions are not artefacts resulting from the type of measurement performed.

While patterns on the pad detector were generally measured with a total of 1.3×10^6 - 6.9×10^6 events, the acquired statistics were increased to 4.7×10^6 - 1.9×10^7 events for the Timepix. Due to the small 55 µm pixel size of the 512×512 pixel Timepix (compared to 1.3 mm for the pad), the number of events in each pixel was hence only in the range of 18-72 events, which, however, is still sufficient for chi square fit procedures, as was outlined in Ref. [26]. The channeling and blocking features visible in the Timepix patterns in the as-implanted and annealed state are essentially the same as discussed for the pad detector, as are the results of the lattice location analysis.

6. Measurement results of GaN sample #2 with the pad detector

For completeness, we present also the experimental and best fit patterns measured for GaN sample #2, in the as-implanted at RT state (Fig. S11) and following 900°C annealing (Fig. S12). The channeling and blocking features are very similar to the measurements performed for GaN sample #1. However, since the ^{24}Na fluence implanted in GaN #2 (4.8×10^{12} cm^{-2}) was considerably lower than in GaN #1 (2.9×10^{13} cm^{-2}), the acquired number of counts had to be reduced for some of the measurements, resulting in patterns with increased Poisson noise, e.g. Fig. S12 (c).

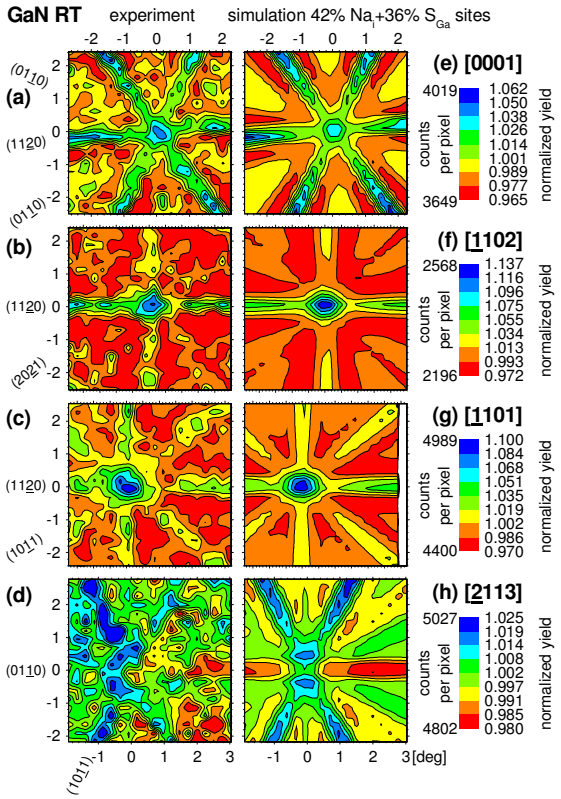

FIG. S11. (a)-(d) Angular distribution of β⁻ emission yields from ^{24}Na in GaN sample #2, measured as-implanted at RT with the pad detector #2. Patterns are shown as contour plots around the [0001], [–1102], [–1101] and [–2113] axes, with the color scales indicating both number of counts per pixel and the normalized yields. The approximate numbers of events measured were 1.8×10^6 (a), 1.1×10^6 (b), 2.2×10^6 (c), and 2.4×10^6 (d). (e)-(h): the best fit of simulated patterns, corresponding to 42(9)% on Na$_i$ interstitial and 36(5)% on S$_{Ga}$ sites.

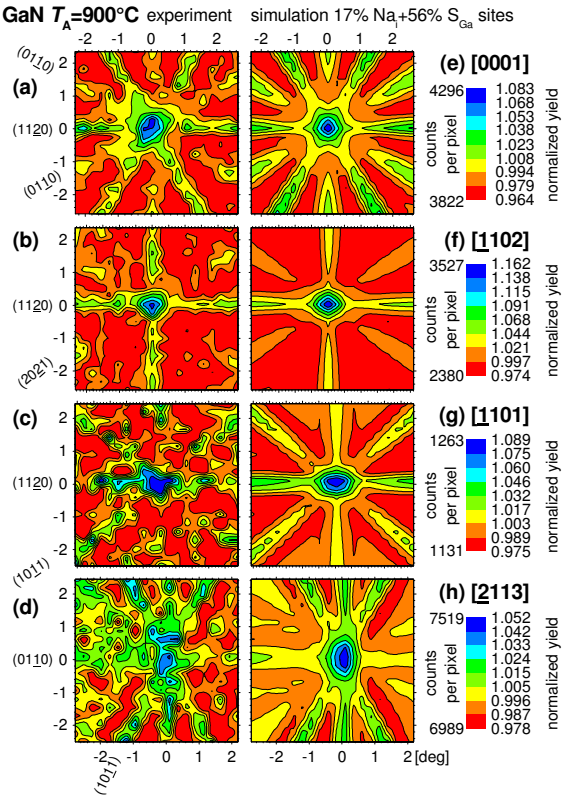

FIG. S12. Same as Fig. S11 but measured following annealing at T_A=900°C. (a)-(d) are experimental patterns while (e)-(h) show the best fit of simulated patterns, corresponding to 17(10)% on Na$_i$ interstitial and 56(4)% on S$_{Ga}$ sites. The approximate numbers of events measured were 1.9×10^6 (a), 1.1×10^6 (b), 0.5×10^6 (c), and 3.5×10^6 (d).

7. Additional comments on experimental patterns from the AlN sample in Figs 4 and 5 of main paper

Compared to GaN, the planar channeling effects in the AlN measurements in Figs 4 and 5 of main paper are much less visible. There are several reasons for that:
a) The relative intensity of axial and planar effects from substitutional sites in AlN is different from that in GaN: compared to the axial effects, planar effects tend to be less intense in AlN than in GaN. This is a consequence of the more rigid lattice of AlN in combination with the lower *Z* of Al compared to Ga, which tends to make axial dechanneling less pronounced in AlN. As a result of this, when the color scales of patterns are adjusted to the strength of the axial effects, planar effects are less prominently visible in AlN, cf. the theoretical patterns in Fig. S7.
b) Due to the lower structural quality of the AlN sample resulting from larger mosaic spread compared to GaN, all channeling effects in the AlN sample are reduced in intensity, i.e. the overall anisotropy is smaller than for a perfect crystal.
c) The scattered electron background for the setup/detector combination used in the AlN measurements (pad detector #2) was higher than for those used for GaN (pad detector #4 and #6), causing increased Poisson noise.
d) Due to the decrease in sample activity towards the end of the experiment, some of the patterns following 900°C annealing had to be measured with less statistics than in the as-implanted case, which, due to increased Poisson noise, does not help with improving the visibility of the planar effects.

8. Comments on possible influence of GaN doping type

In our investigations on the lattice sites of ^{27}Mg in GaN [19, 34] we were able to show that the interstitial *vs* substitutional Mg fractions depend on the doping type (in *p*-GaN, interstitial ^{27}Mg was found to be much more prominent than *n*-GaN). Similar results were meanwhile also obtained in the case of ^{11}Be (as yet unpublished). From the technological point of view, it is highly interesting to study the related compensation mechanism of Mg acceptors, and much theoretical work has also been performed on the case of Be, however, this issue is less relevant for Na as a double acceptor. While for fundamental reasons it would also be worthwhile to study it for ^{24}Na, we did not attempt this for the following reasons. Our experiments with Mg revealed that the initial, i.e. as-grown, *p*- or *n*-doping type of GaN is pushed towards intrinsic conditions by the compensating nature of implantation damage, and this strong compensation occurs already for low fluences, so that implantations above 1×10^{12} cm^{-2} basically can only probe the situation in undoped GaN. Note that staying below 10^{12} cm^{-2} would mean to reduce implanted fluences by at least a factor of 10 compared to the experiments described in this manuscript. It is easily possible to access this ultra-low fluence regime $<10^{12}$ cm^{-2} in on-line experiments with short-lived isotopes such as ^{27}Mg ($t_{1/2}$=9.47 min) or ^{11}Be (13.8 s), e.g. by continuously measuring the development of a [0001] pattern as a function of implanted fluence. However, for a long-lived isotope like ^{24}Na (14.96 h) count rates become very small for fluences $< 10^{12}$ cm^{-2}, making such experiments rather challenging and time-consuming.

9. Comments on expected accuracy and precision of the location of the interstitial Na site

Naturally, one of our goals is also to critically assess the *accuracy* and *precision* of the emission channeling lattice location results that can be achieved. The *accuracy*, however, is difficult to judge since emission channeling is the only experimental method that can give information on the lattice sites of such impurities as Mg, Be, or Na in nitride semiconductors, so that our results can only be compared with theoretical predictions. As what regards the *precision*, it is quite clear that a comparison of the emission channeling results of different crystallographic directions of the same sample provides a limit to the precision that has been reached, since it cannot be better than the scatter of individual measurements. With respect to the location of the interstitial site, the precision critically depends on the amount of probe atoms that are found on this site, since this determines the "contrast" visible in the patterns. This is illustrated by the case of ^{24}Na in ZnO (which possesses the same wurtzite structure as GaN): there, 40-70% of ^{24}Na was found on interstitial sites and the results for the position of the interstitial site derived from different measurements and different samples scattered by less than 0.10 Å [21]. In the case of ^{27}Mg in GaN [19, 33], where detailed lattice location could only be performed for conditions with ~13% interstitial ^{27}Mg, the scatter was ~0.40 Å. For ^{24}Na in GaN, with interstitial fractions of ~38-45% at RT, we are in between these two situations, so a scatter in the results of ~0.20 Å (as is observed in between the two samples GaN #1 and #2) would be no surprise at all. However, what we observe is that the RT results of sample #1 scatter by only 0.10 Å (although being measured by two different detection methods) and those of #2 by only 0.03 Å. Due to the limited number of measurements, this may of course simply be coincidence, but it could also have systematic reasons, and it seemed worthwhile to us mentioning this as a possible and interesting hypothesis, without any proof. However, we are not of the opinion that at this point it warrants extensive additional characterization of the samples, especially since – if the effect should be real – we can only speculate about possible reasons. As such we may mention e.g. the possibility of different strain environments around the implanted ^{24}Na probes, which may be caused by the different mosaic spread of the two samples or by the difference in implantation fluence.